INTERNATIONAL JOURNAL FOR NUMERICAL METHODS IN FLUIDS
Int. J. Numer. Meth. Fluids **31**: 861–877 (1999)

MIXED BOUNDARY ELEMENTS FOR LAMINAR FLOWS

MATJAŽ RAMŠAK* AND LEOPOLD ŠKERGET

Faculty of Mechanical Engineering, University of Maribor, Smetanova 17, SI-2000 Maribor, Slovenia

SUMMARY

This paper presents a mixed boundary element formulation of the boundary domain integral method (BDIM) for solving diffusion–convective transport problems. The basic idea of mixed elements is the use of a continuous interpolation polynomial for conservative field function approximation and a discontinuous interpolation polynomial for its normal derivative along the boundary element. In this way, the advantages of continuous field function approximation are retained and its conservation is preserved while the normal flux values are approximated by interpolation nodal points with a uniquely defined normal direction. Due to the use of mixed boundary elements, the final discretized matrix system is overdetermined and a special solver based on the least squares method is applied. Driven cavity, natural and forced convection in a closed cavity are studied. Driven cavity results at $Re = 100$, 400 and 1000 agree better with the benchmark solution than Finite Element Method or Finite Volume Method results for the same grid density with 21×21 degrees of freedom. The average Nusselt number values for natural convection $10^3 \leq Ra \leq 10^6$ agree better than 0.1% with benchmark solutions for maximal calculated grid densities 61×61 degrees of freedom. Copyright © 1999 John Wiley & Sons, Ltd.

KEY WORDS: incompressible viscous flow; velocity–vorticity formulation; boundary element method

1. INTRODUCTION

The velocity–vorticity formulation of Navier–Stokes equations for the boundary domain integral method (BDIM) was introduced by Wu [1] and Škerget *et al.* [2]. The main advantage of the velocity–vorticity formulation of the Navier–Stokes equations is the numerical separation of kinematic and kinetic aspects of the fluid flow from the pressure computation. Since the pressure does not appear explicitly in the field functions conservation equations, the well-known difficulty arising from the computation of the boundary pressure values in incompressible fluid motion is avoided. In the BDIM, the surface vorticity is computed directly from the kinematic computation.

To accelerate the convergence and stability of the coupled velocity–vorticity iterative scheme, the false transient approach is applied to the kinematic equation rendering it to the parabolic partial differential equation (PDE), see [3,4].

The main restriction of the classic BDIM for fluid dynamics is the availability of the fundamental solutions for PDE with constant coefficients only. The problem can be solved by locally partitioning the non-linear coefficients into constant and variable parts, see Žagar and Škerget [5], Rek and Škerget [6]. However, if the whole domain is treated as one, the system

* Correspondence to: Faculty of Mechanical Engineering, University of Maribor, Smetanova 17, SI-2000 Maribor, Slovenia.

CCC 0271–2091/99/210861–17$17.50

Received March 1998
Revised July 1998

matrix is full and non-symmetric, and therefore cumbersome to solve. Both problems can be eliminated by decomposing the whole domain into subdomains. In the extreme case of domain decomposition, e.g. each subdomain is one cell surrounded by four boundary elements, and different material properties can be applied to each subdomain, see Zagar and Škerget [7]. The system matrices are sparse and well suited to modern iterative solution methods, see Hribersek and Škerget [8].

The derivative of the field function in the normal direction to the boundary element ('flux') is computed explicitly from discretized BDIM integral equations in implicit matrix system. For this reason the unit normal vector in the flux interpolation nodal point has to be known. In the rectangular subdomain vertex the normal direction is undefined. This problem is solved by using the discontinuous approximation for the function and the flux [2], see Figure 2. By definition, the first and major disadvantage is the discontinuous field function approximation and, therefore, the conservative field function is not preserved. The second disadvantage is a significant increase in the number of nodal points, which slows down the rate of solution convergence and increasing the computer memory demands. The third disadvantage is the non-unique approximation of the field function over the subdomain with the increased number of boundary nodal points, see [9].

The idea of mixed elements, presented in this paper, represents an alternative approach in BDIM. The basic idea of mixed elements is to split the field function and flux nodal points to keep the advantages of function continuous approximation and to avoid the undefined normal directions of flux interpolation nodal points. Therefore, the function is approximated with continuous interpolation polynomials while flux is interpolated with discontinuous interpolation polynomials. As a consequence, the advantages of continuous field function approximations are retained and its conservation is preserved while the normal flux values are modelled in a proper way. When using continuous elements of high orders, the application of the matching conditions of common interfaces, i.e. the matrix assembly, leads to an overdetermined system of algebraic equations. Instead of using one of the several schemes that reduce the overdetermined system to a closed system, see Banerjee and Butterfield [10], the overdetermined system matrix is solved in a least squares sense.

The aim of the present work is to show an efficient use of the mixed elements in BDIM for a velocity–vorticity formulation of Navier–Stokes equations. In Section 2, the governing equations are stated and in Section 3, the numerical solution with BDIM is presented. In order to test the validity and effectiveness of mixed elements in BDIM several test examples were computed. In Section 4, the first test example is a driven cavity with velocity and vorticity profiles compared with benchmark solutions by Ghia *et al.* [11] and two other commercial programmes. In Section 5, the test case is a natural convection in a closed cavity, where an average Nusselt number value is compared with a benchmark solution by Davis [12]. The last test example in Section 6 is a mixed convection in a cavity, e.g. natural and forced convection. The results are compared with results obtained by the finite element method (FEM) by Lee and Chen [13].

2. GOVERNING EQUATIONS

The Navier–Stokes equations for plane viscous incompressible fluid flow can be written in velocity–vorticity formulation for kinematics, kinetics and heat energy transport respectively, see Škerget *et al.* [2].

$$\frac{\partial^2 v_i}{\partial x_j \partial x_j} + e_{ij}\frac{\partial w}{\partial x_j} - \frac{1}{\alpha}\frac{\partial v_i}{\partial t} = 0,$$

$$\frac{\mathrm{D}\omega}{\mathrm{D}t} = \frac{\partial \omega}{\partial t} + v_j \frac{\partial \omega}{\partial x_j} = \nu \frac{\partial^2 w}{\partial x_j \partial x_j} + e_{ij} g_j \frac{\partial F}{\partial x_i}, \tag{1}$$

$$\frac{\mathrm{D}T}{\mathrm{D}t} = \frac{\partial T}{\partial t} + v_j \frac{\partial T}{\partial x_j} = \kappa \frac{\partial^2 T}{\partial x_j \partial x_j} + \frac{I}{\rho c_p},$$

where v_i is Cartesian velocity, ω is the vorticity, T is the temperature, e_{ij} is the unit permutation symbol, $F = \beta(T - T_0)$ is the Boussinesq approximation of the buoyancy effect, g_i is the gravity, ν is the viscosity, κ is the thermal diffusivity, ρ is the fluid density, c_p is the specific isobaric heat and I is the source of heat generation.

To accelerate convergence and stability of the coupled velocity–vorticity iterative scheme, the false transient approach is applied to the kinematic equation, rendering it to parabolic PDE satisfied only at $t \to \infty$, with α treated as a relaxation parameter, see [4].

2.1. Boundary conditions

Boundary conditions in kinematics and heat energy transport can be Dirichlet, Neumann or Cauchy, while boundary conditions $\omega \in \Gamma$ used in kinetics are Dirichlet calculated directly from kinematic results as a curl of the velocity field [9].

$$\omega = e_{ij}\frac{\partial v_i}{\partial x_j}.$$

3. NUMERICAL SOLUTION

3.1. Integral representation of parabolic diffusion–convective equation

Transport equations for kinematics, kinetics and heat energy transport (1) can be written in a general form as

$$a\frac{\partial^2 u}{\partial x_j \partial x_j} - \frac{\partial u}{\partial t} - \frac{\partial v_j u}{\partial x_j} + \frac{\partial f_j}{\partial x_j} + I = 0, \tag{2}$$

where u is conservative field function, a is the diffusivity coefficient and I is the source term. Boundary conditions on Γ and initial conditions in domain Ω have to be known

$$u = \bar{u}, \quad \frac{\partial u}{\partial n} = \overline{\frac{\partial u}{\partial n}} \qquad \text{in } \Gamma \text{ for } t \geq t_0, \tag{3}$$

$$u = \bar{u}_0 \qquad \text{in } \Omega \text{ for } t = t_0. \tag{4}$$

By using a finite difference approximation of the field function time derivative for the time increment $\Delta t = t_F - t_{F-1}$, e.g.

$$\frac{\partial u}{\partial t} \approx \frac{u_F - u_{F-1}}{\Delta t}, \tag{5}$$

the differential formulation can be transformed into an equivalent integral statement by Green's theorems for scalar functions, see Škerget [9].

$$c(\xi)u(\xi)+\int_\Gamma u\frac{\partial u^*}{\partial n}\,\mathrm{d}\Gamma$$
$$=\int_\Gamma \frac{\partial u}{\partial n}u^*\,\mathrm{d}\Gamma-\frac{1}{a}\int_\Gamma uv_jn_ju^*\,\mathrm{d}\Gamma+\frac{1}{a}\int_\Omega uv_j\frac{\partial u^*}{\partial x_j}\,\mathrm{d}\Omega+\frac{1}{a}\int_\Gamma f_jn_ju^*\,\mathrm{d}\Gamma-\frac{1}{a}\int_\Omega f_j\frac{\partial u^*}{\partial x_j}\,\mathrm{d}\Omega$$
$$+\frac{1}{a}\int_\Omega Iu^*\,\mathrm{d}\Omega+\beta\int_\Omega u_{F-1}u^*\,\mathrm{d}\Omega, \tag{6}$$

where n_j is the normal direction to the nodal point. The variable u^* is the modified Helmholtz fundamental solution, i.e. the solution of equation

$$\frac{\partial^2 u^*}{\partial x_j\,\partial x_j}-\mu^2u^*+\delta(\xi,s)=0, \tag{7}$$

and given for the plane case as

$$u^*=\frac{1}{2\pi}K_0(\mu r),$$
$$\frac{\partial u^*}{\partial x_j}n_j=\frac{r_jn_j}{2\pi r^2}\mu rK_1(\mu r), \tag{8}$$

where the parameter μ is defined as

$$\mu^2=\frac{1}{a\Delta t}=\beta. \tag{9}$$

K_0 and K_1 are the modified Bessel functions of the second kind and $r_j(\xi, s)$ is the vector from the source point ξ to the reference field point s, e.g. $r_j=x_j(\xi)-x_j(s)$ for $j=1, 2$, while r is its magnitude $r=|r_j|$.

Other fundamental solutions can be applied, e.g. elliptic diffusion–convective, but in all presented numerical examples the modified Helmholtz fundamental solution is used.

3.2. Discretization

The solution domain is discretized in subdomains, as in the FEM or the finite volume method (FVM), e.g. each subdomain is surrounded by four boundary elements. The quadratic discrete model is presented in Figure 1.

With the discontinuous approximations of flux $\partial u/\partial n$, the undefined normal in the vertex points of a subdomain is avoided. Boundary element interpolation polynomials can be split for

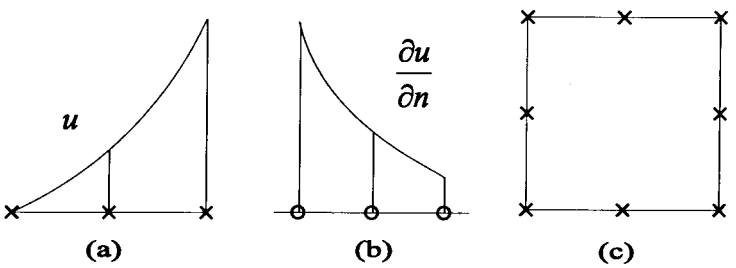

Figure 1. Discretization: (a) continuous quadratic interpolation of u, (b) discontinuous quadratic interpolation of $\partial u/\partial n$ along boundary element, (c) continuous quadratic interpolation of function in subdomain. × represents a u nodal points, while ○ represents a $\partial u/\partial n$ nodal point.

field function Φ_u^n and its flux Φ_q^n, see caption in Figure 1, where the index n refers both to the number of interpolation nodes in each boundary element or subdomain and to the degree of the respective interpolation polynomial.

The interpolation polynomials for function approximation over the boundary element ($\xi, \eta \in [-1, 1]$ being local co-ordinates) are given with the expressions

$$\Phi_u^n = \frac{1}{2}\begin{Bmatrix} -\xi + \xi^2 \\ 1 - \xi^2 \\ \xi + \xi^2 \end{Bmatrix},$$

while flux is approximated with

$$\Phi_q^n = \frac{1}{9}\begin{Bmatrix} -6\xi + 8\xi^2 \\ 9 + 16\xi^2 \\ 6\xi + 8\xi^2 \end{Bmatrix}.$$

Domain approximation is biquadratic,

$$\phi^n = \frac{1}{4}\begin{Bmatrix} -1 + \xi\eta + \xi^2 + \eta^2 - \xi^2\eta - \xi\eta^2 \\ 2 - 2\eta - 2\xi^2 + 2\xi^2\eta \\ -1 - \xi\eta + \xi^2 + \eta^2 - \xi^2\eta + \xi\eta^2 \\ 2 + 2\xi - 2\eta^2 - 2\xi\eta^2 \\ -1 + \xi\eta + \xi^2 + \eta^2 + \xi^2\eta + \xi\eta^2 \\ 2 + 2\eta - 2\xi^2 - 2\xi^2\eta \\ -1 - \xi\eta + \xi^2 + \eta^2 + \xi^2\eta - \xi\eta^2 \\ 2 - 2\xi - 2\eta^2 + 2\xi\eta^2 \end{Bmatrix}.$$

With the integrals of fundamental solution u^* being

$$h^n = \int_{\Gamma_e} \Phi_u^n \frac{\partial u^*}{\partial n}\, d\Gamma, \qquad g^n = \int_{\Gamma_e} \Phi_q^n u^*\, d\Gamma,$$

$$g_j^n = \int_{\Gamma_e} n_j \Phi_u^n u^*\, d\Gamma,$$

$$d_j^n = \int_{\Omega_c} \phi^n \frac{\partial u^*}{\partial x_j}\, d\Omega, \qquad d^n = \int_{\Omega_c} \phi^n u^*\, d\Omega, \tag{10}$$

which are the functions of the geometry, time increment and material properties, representing the integration over individual boundary element or subdomain, the following discretized equation can be written, corresponding to the integral equation (6),

$$\begin{aligned} c(\xi)u(\xi) + \sum_{e=1}^{E} \{h\}^T\{u\}^n = {} & \sum_{e=1}^{E} \{g\}^T \left\{\frac{\partial u}{\partial n}\right\}^n - \frac{1}{a}\sum_{e=1}^{E} \{g_j\}^T\{uv_j\}^n + \frac{1}{a}\sum_{c=1}^{C} \{d_j\}\{uv_j\}^n \\ & + \frac{1}{a}\sum_{e=1}^{E} \{g_j\}^T\{f_j\}^n - \frac{1}{a}\sum_{c=1}^{C} \{d_j\}^T\{f_j\}^n + \frac{1}{a}\sum_{c=1}^{C} \{d\}^T\{I\}^n \\ & + \beta \sum_{c=1}^{C} \{d\}^T\{u\}_{F-1}^n. \end{aligned} \tag{11}$$

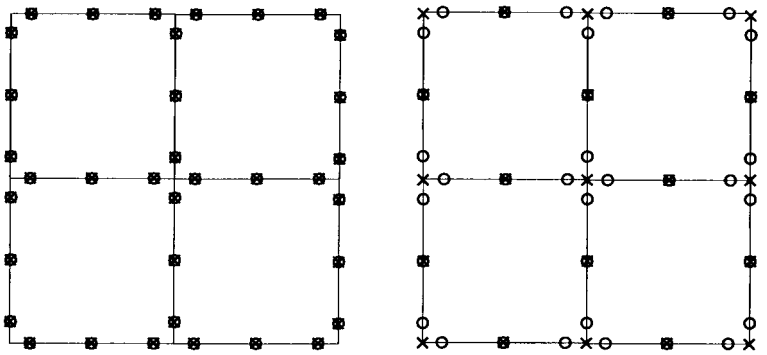

Figure 2. Classic BDIM quadratic subdomains (left) and mixed BDIM subdomains (right). × represents a u nodal points, while ○ represents a $\partial u/\partial n$ nodal point.

Applying Equation (11) to all unknown boundary nodes, functions and fluxes for each subdomain, the following rectangular implicit matrix system is obtained:

$$\left([H]+\frac{1}{\bar{a}}\left([G_j-D_j][v_j]\right)\right)\{u\}=[G]\left\{\frac{\partial u}{\partial n}\right\}+\frac{1}{\bar{a}}[G_j-D_j]\{f_j\}+\frac{1}{\bar{a}}[D]\{I\}+\beta[D]\{u\}_{F-1}. \tag{12}$$

3.3. Interface boundary conditions

Accounting for the boundary conditions in Equation (3) and the compatibility and equilibrium interface conditions between subdomains I and II

$$u|_{\mathrm{I}}=u|_{\mathrm{II}}, \qquad \left.\frac{\partial u}{\partial n}\right|_{\mathrm{I}}=-\left.\frac{\partial u}{\partial n}\right|_{\mathrm{II}}, \tag{13}$$

the following system is obtained:

$$[A]_{M\times N}\{x\}_N=\{F\}_M, \tag{14}$$

where M is the number of equations and N is the number of unknowns. The resulting system of equations has more equations than unknowns, hence it should be solved using a special algorithm.

In the classic BDIM formulation, the nodal points for the field function and the flux interpolation are the same, Figure 2 (left), and always between two subdomains. For each nodal point between two subdomains, two unknown values exist (function and flux), and two discretized subdomain integral equations, one from both neighbouring subdomains needs to be solved. After coupling them with interface boundary conditions (13) the resulting system shows two discretized integral equations with two unknowns.

The extension of this principle for mixed boundary elements is not straightforward. First, the vertex point of a subdomain can be surrounded by four subdomains. Second, at the nodal point, one value is unknown, either the function or the normal flux, Figure 2 (right), but at least two equations are available from each neighbouring subdomain. If the classic procedure is followed, then at least one equation is lost at each nodal point and the results are false. To keep the influence of all related subdomains, the equations must be confined to a system that produces an overdetermined system.

3.4. Solver

One of the simplest approaches for solving an overdetermined set of algebraic equations (14), where is $M > N$, is finding a least squares solution using QR decomposition of $A = Q \cdot R$, where R is upper triangular and Q is orthogonal matrix ('gen. LLS') [14]. Since, in this case, the system matrix A is sparse and block banded, the iterative linear least squares solver (LLS) of Paige and Saunders (iter. LLS) [15] is much faster at the same solution accuracy. Only the non-zero elements have to be stored in computer memory, therefore, much larger problems can be solved.

Generalized and iterative solvers are compared for solving of a diffusion–convective problem known as an entry flow, Table I. The solution residuum is calculated as

$$\text{res} = \frac{\|Ax - b\|_2}{\|b\|_2}, \tag{15}$$

where x is the obtained solution.

4. NATURAL CONVECTION IN A CLOSED CAVITY

4.1. Problem definition

The problem considered is that of a two-dimensional flow of a Boussinesq fluid for Prandtl number 0.71 in an upright square cavity described in non-dimensional terms $0 \leq x \leq 1$ and $0 \leq y \leq 1$, with y upwards. Both velocity components are zero on the boundaries. The horizontal walls are isolated and the vertical sides are at temperatures $\bar{T} = 1$ and $\bar{T} = 0$. Due to the buoyancy force, the fluid begins to rotate. Geometry and boundary conditions are presented in Figure 3.

The solution of this problem (velocities, temperature and rates of heat transfer) was obtained for Rayleigh numbers of values 10^3, 10^4, 10^5 and 10^6. The problem statement is the same as in Davis and Jones [12].

The BDIM is compared with benchmark solutions by Davis, which are obtained from different grid densities up to 81×81 points and their extrapolation to infinite density. The accuracy of BDIM is compared with Davis and FEM at the same number of degrees of freedom for function per domain of solution. FEM results are obtained with the equal grids of 9-node quadratic elements, equidistant and non-equidistant as described in Exercise 7 in the FIDAP Examples Manual (Fluid Dynamics International) [16]. Extreme values of velocities

Table I. Comparison of generalized and iterative linear least squares solver

Matrix parameters				Gen. LLS		Iter. LLS	
N_{sub}	M	N	Sparse	res	CPU	res	CPU
16	216	111	0.124	0.00024	0.17	0.00003	0.26
64	944	447	0.033	0.00005	23.0	0.00002	1.8
256	2184	1007	0.015	0.00001	1435.0	0.00002	15.0
1024	16 128	9215	0.002	—	—	0.00027	67.0

N_{sub} means number of subdomains, M and N are the number of equations and unknowns respectively, the sparse coefficient is calculated as the number of non-zero elements in a matrix divided by $M * N$, res is the normalized solution residuum, see Equation (15).

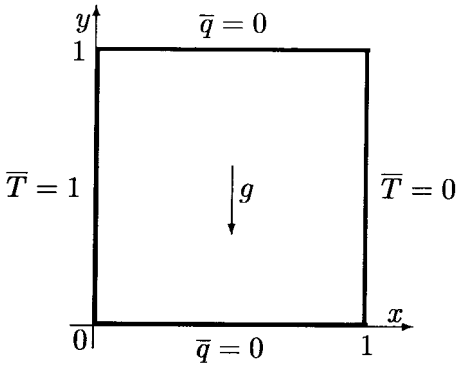

Figure 3. Geometry and boundary conditions for natural convection.

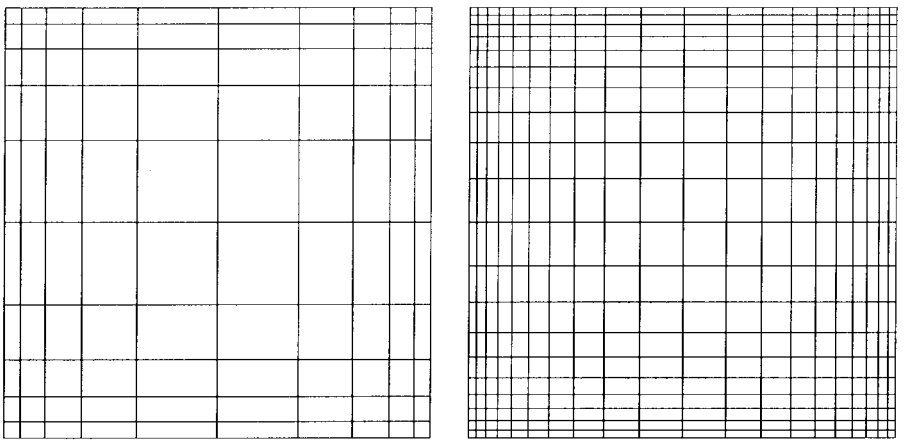

Figure 4. Grid density 21×21 dof and 41×41 dof with a ratio longest/shortest = 6.

are obtained with interpolation between grid points at Davis and BDIM, while the FEM results are obtained at grid points without interpolation.

4.2. Results

Computations are performed for different grid densities, equidistant and non-equidistant grids with a ratio of 6 between the longest and the shortest element, see Figure 4. In Tables II, III, IV and V, the following results are presented:

N_{sub}	number of subdomains in BDIM, while at FEM number of elements
N_{dof}	number of degrees of freedom for function
$v_{x,\max}$	the maximum horizontal velocity on the vertical mid-plane of the cavity and
y	as its location at grid point;
$v_{y,\max}$	the maximum vertical velocity on the horizontal mid-plane of the cavity and
x	as its location at grid point;
$\overline{Nu}$	the average Nusselt number value throughout the cavity;
Nu_0	the average Nusselt number value on the left vertical boundary of the cavity at $x = 0$.

The formulation for a modified Helmholtz fundamental solution is used. The steady state is computed for cases with $Ra = 10^3$, 10^4 and 10^5, with one time step $\Delta t = 10^{16}$ and with a different underrelaxation factor for vorticity kinetics 1.0, 0.1, 0.01 respectively. The steady state for $Ra = 10^6$ is computed as a transient case with $\Delta t = 10^{-3}$ and 0.5 as an

Table II. Natural convection at $Ra = 10^3$, quadratic discretization, equidistant grid

	Davis		FEM	BDIM			
N_{sub}			10×10	6×6	10×10	20×20	30×30
N_{dof}	Bench	21×21	21×21	13×13	21×21	41×41	61×61
$v_{x,max}$	3.649	3.589	3.634	3.593	3.648	3.649	3.649
y	0.813	0.811	0.800	0.815	0.815	0.813	0.813
$v_{y,max}$	3.697	3.629	3.660	3.643	3.698	3.696	3.697
$\underline{x}$	0.178	0.181	0.200	0.158	0.178	0.179	0.179
$\overline{Nu}$	1.118	1.111	1.120	1.117	1.117	1.118	1.118
Nu_0	1.117	1.113	1.120	1.117	1.117	1.118	1.118

Table III. Natural convection at $Ra = 10^4$, quadratic discretization, equidistant grid

	Davis		FEM	BDIM			
N_{sub}			10×10	6×6	10×10	20×20	30×30
N_{dof}	Bench	21×21	21×21	13×13	21×21	41×41	61×61
$v_{x,max}$	16.178	16.189	15.987	16.040	16.190	16.168	16.181
y	0.823	0.820	0.800	0.842	0.823	0.822	0.823
$v_{y,max}$	19.617	19.197	19.268	20.262	19.351	19.596	19.627
$\underline{x}$	0.119	0.125	0.100	0.121	0.121	0.120	0.119
$\overline{Nu}$	2.243	2.212	2.297	2.270	2.244	2.243	2.243
Nu_0	2.238	2.255	2.297	2.270	2.244	2.243	2.243

Table IV. Natural convection at $Ra = 10^5$, quadratic discretization, equidistant grid

	Davis		FEM	BDIM			
N_{sub}			10×10	6×6	10×10	20×20	30×30
N_{dof}	Bench	21×21	21×21	13×13	21×21	41×41	61×61
$v_{x,max}$	34.73	36.46	33.93	37.09	34.74	34.92	34.71
y	0.855	0.854	0.850	0.870	0.856	0.855	0.850
$v_{y,max}$	68.59	62.79	65.65	70.67	67.75	68.61	68.59
$\underline{x}$	0.066	0.075	0.050	0.088	0.068	0.065	0.060
$\overline{Nu}$	4.519	4.454	4.895	4.721	4.493	4.504	4.515
Nu_0	4.509	4.716	4.895	4.720	4.493	4.492	4.515

Table V. Natural convection at $Ra = 10^6$, quadratic discretization, non-equidistant grid, ratio longest/shortest = 6

	Davis		FEM	BDIM			
N_{sub}			10×10	6×6	10×10	20×20	30×30
N_{dof}	Bench	21×21	21×21	13×13	21×21	41×41	61×61
$v_{x,max}$	64.63	79.27	335.56	—	69.33	64.45	64.55
y	0.850	0.862	0.754	—	0.887	0.861	0.849
$v_{y,max}$	219.36	195.44	198.17	—	215.73	220.07	220.54
x	0.038	0.045	0.039	—	0.034	0.037	0.038
$\overline{Nu}$	8.800	9.027	7.653	—	8.852	8.763	8.808
Nu_0	8.817	9.502	7.652	—	8.797	8.769	8.808

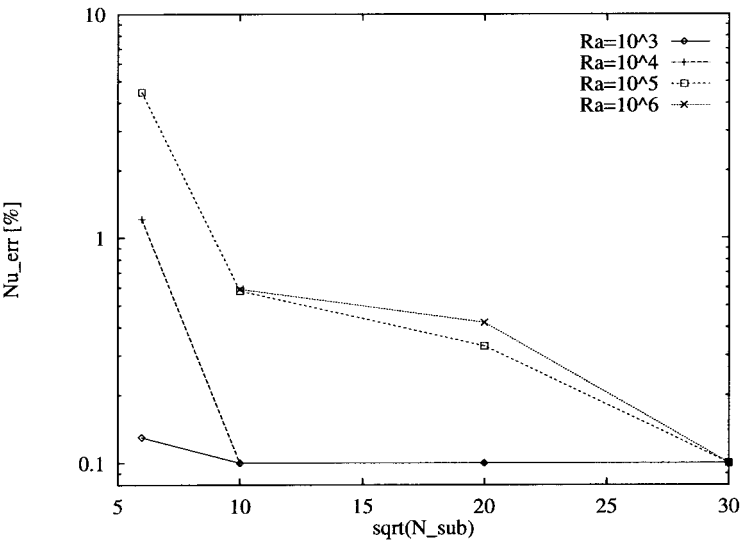

Figure 5. Average Nusselt number error of BDIM against a grid density for different *Ra* numbers.

underrelaxation factor. The convergence criteria for all runs have been 10^{-4}. Figure 5 shows the average Nusselt number error computed as

$$Nu_{err} = \frac{|\overline{Nu_i} - \text{Bench}|}{\text{Bench}} \times 100$$

against a grid density. It is obvious that the results converge to a benchmark solution. Keep in mind that, for $Ra = 10^6$, the grid is non-equidistant, resulting in a smaller error value than at equidistant grid for $Ra = 10^5$.

An accuracy comparison between the finite difference method of Davis, the finite element method and the BDIM is presented in Figure 6, where the average Nusselt number error is plotted against the *Ra* number at the same grid density of 21×21 dof. The BDIM results agree the best to benchmark solution, except at $Ra = 10^5$, where it is very close to Davis.

5. DRIVEN CAVITY FLOW

5.1. Problem definition

The problem considered here is that of a square cavity totally filled with an incompressible viscous fluid and a moving bottom wall at a constant velocity. Geometry and boundary conditions are presented in Figure 7.

The test case is used because many results have been obtained by different authors using different numerical approaches. The results are compared using the work of Ghia *et al.* [11] as a benchmark solution to this problem. The test case was solved using two commercial codes: the FIDAP (Fluid Dynamics International) with the FEM and the TASCflow (Advanced Scientific Computing) [17] with the FVM; therefore, we can now make a comparison of the three different methods on an equal grid with the same number of degrees of freedom.

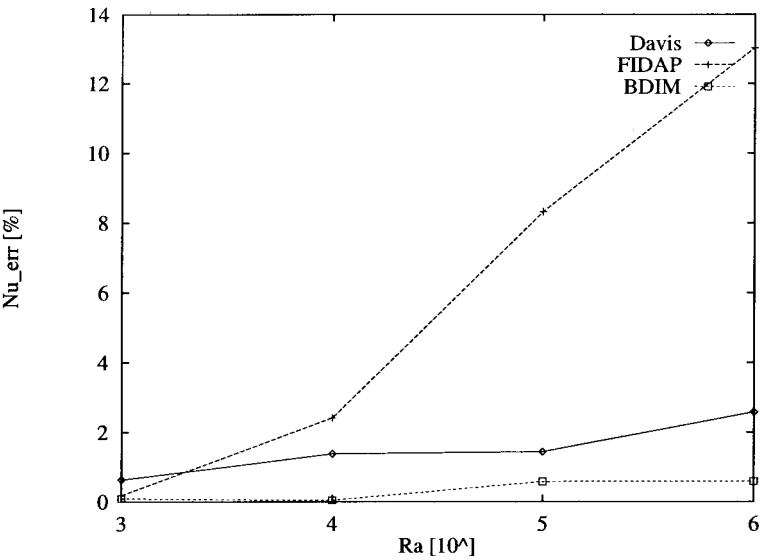

Figure 6. Average Nusselt number error comparison between the finite difference method of Davis, FEM and BDIM at the same grid density of 21×21 dof.

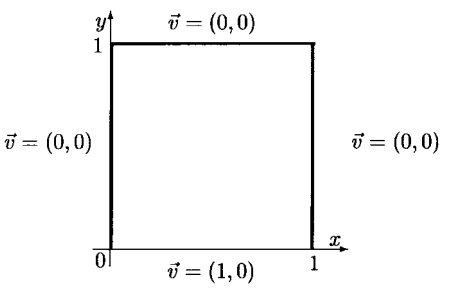

Figure 7. Geometry and boundary conditions for a driven cavity.

Table VI. Driven cavity at $Re = 100$; comparison of extreme values with the benchmark values of Ghia

	dof	l/s	$v_x-\min$	$v_y-\max$	$v_y-\min$
FEM	21×21	1	-0.178	0.217	-0.152
FVM	21×21	1	-0.191	0.233	-0.160
BDIM	21×21	1	-0.213	0.259	-0.177
BDIM	21×21	6	-0.219	0.254	-0.183
BDIM	41×41	1	-0.214	0.254	-0.179
Ghia	129×129	1	-0.211	0.245	-0.175

Table VII. Driven cavity at $Re = 400$; comparison of extreme values with the benchmark values of Ghia

	dof	l/s	$v_x-\min$	$v_y-\max$	$v_y-\min$
FEM	21×21	6	-0.286	0.405	-0.261
FVM	21×21	6	-0.170	0.315	-0.172
BDIM	21×21	6	-0.347	0.451	-0.317
FEM	41×41	6	-0.309	0.430	$-0.284.$
FVM	41×41	6	-0.237	0.387	-0.230
BDIM	41×41	6	-0.327	0.458	-0.306
Ghia	129×129	1	-0.327	0.450	-0.302

Table VIII. Driven cavity at $Re = 1000$; comparison of extreme values with the benchmark values of Ghia

	dof	l/s	$v_x-\min$	$v_y-\max$	$v_y-\min$
FEM	21×21	6	-0.157	0.264	-0.142
FVM	21×21	6	-0.171	0.321	-0.157
BDIM	21×21	6	-0.384	0.503	-0.401
FEM	41×41	6	-0.264	0.359	-0.211
FVM	41×41	6	-0.243	0.411	-0.227
BDIM	41×41	6	-0.389	0.533	-0.371
Ghia	129×129	1	-0.383	0.516	-0.371

5.2. Results

The formulation for a modified Helmholtz fundamental solution is used. The steady state is computed for cases $Re = 100$, 400 and 1000 with one time step $\Delta t = 10^{16}$ and a different underrelaxation factor for vorticity kinetics 0.1, 0.01, 0.001 respectively. The convergence criteria for all runs were 10^{-4}.

The FEM results at $Re = 100$ and 400 are computed without upwinding, while at $Re = 1000$, an upwinding factor of 1.25 was necessary to obtain a good solution.

The FVM results are computed as a transient case with $\Delta t = 10^{-3}$. The convergence criteria was 10^{-6}.

Tables VI, VII and VIII show the minimum velocity v_x along the vertical line through the centre of the cavity and the minimum and maximum velocity v_y along the horizontal line through the centre of the cavity. Extreme values of velocities are obtained with interpolation

between the grid points at BDIM, while the FEM and FVM results are obtained at grid points without interpolation. The velocity profile comparison between FVM, FEM, BDIM and the benchmark solution of Ghia is presented in Figures 8–12 for the same grid densities of 21×21 and 41×41 dof, being equidistant or non-equidistant.

At a low Reynolds number ($Re = 100$, Figure 8), the results are approximately equally accurate, with the slightest advantage being with the BDIM. The BDIM results for the equidistant grid 21×21 dof agree well with the benchmark solution, bearing in mind that the mesh density in the benchmark case was for the grid 129×129 nodes.

At $Re = 400$, Figures 9 and 10, the best results are obtained using the BDIM, followed by the FEM, while the FVM solution differs significantly at both grid densities. The FEM results improved significantly with higher grid densities. The nodalization analysis of the BDIM results between grids 21×21 and 41×41 dof shows very slight profile changes in the direction compared with the benchmark solution (compare Figures 9 and 10).

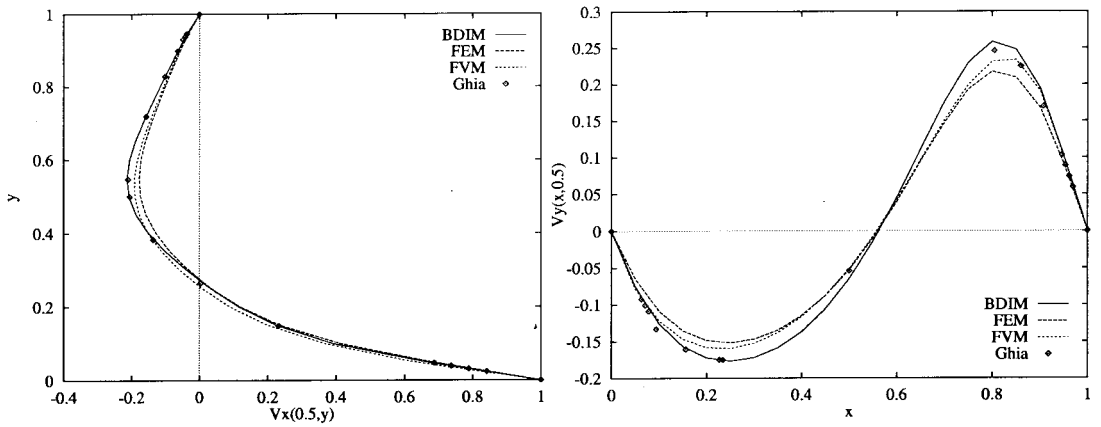

Figure 8. Driven cavity at $Re = 100$. Comparison of BDIM results with FVM, FEM and benchmark solutions by Ghia, horizontal velocity at $x = 0.5$ (left) and vertical velocity at $y = 0.5$ (right). Grid density 21×21 dof with a ratio longest/shortest = 1.

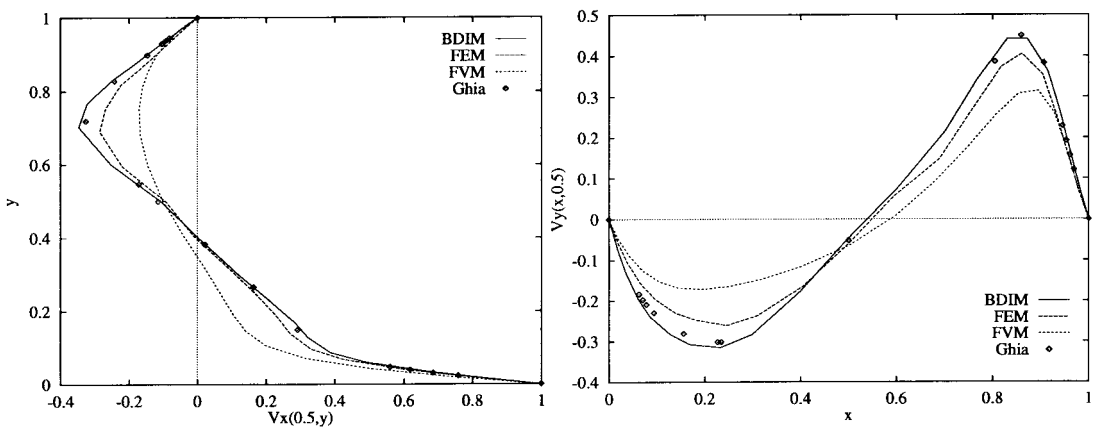

Figure 9. Driven cavity at $Re = 400$. Comparison of BDIM results with FVM, FEM and benchmark solutions by Ghia, horizontal velocity at $x = 0.5$ (left) and vertical velocity at $y = 0.5$ (right). Grid density 21×21 dof with a ratio longest/shortest = 6.

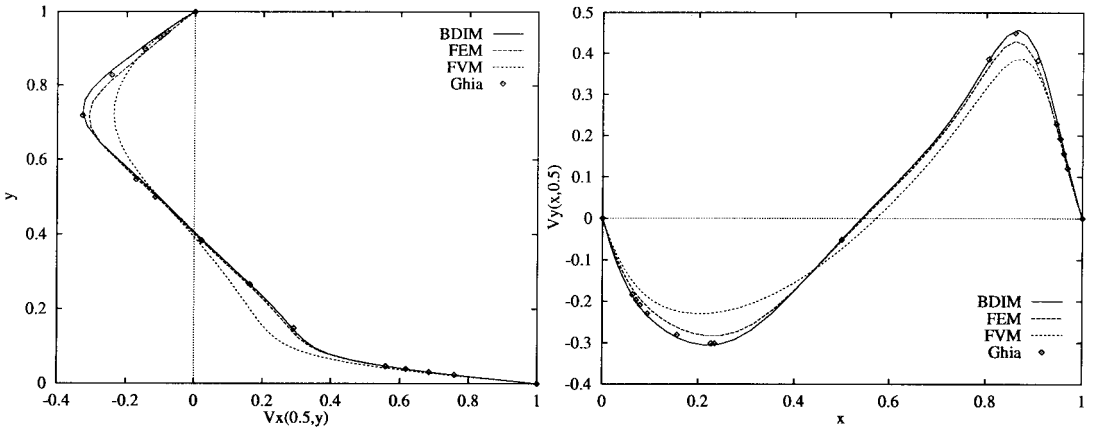

Figure 10. Driven cavity at $Re = 400$. Comparison of BDIM results with FVM, FEM and benchmark solutions by Ghia, horizontal velocity at $x = 0.5$ (left) and vertical velocity at $y = 0.5$ (right). Grid density 41×41 dof with a ratio longest/shortest = 6.

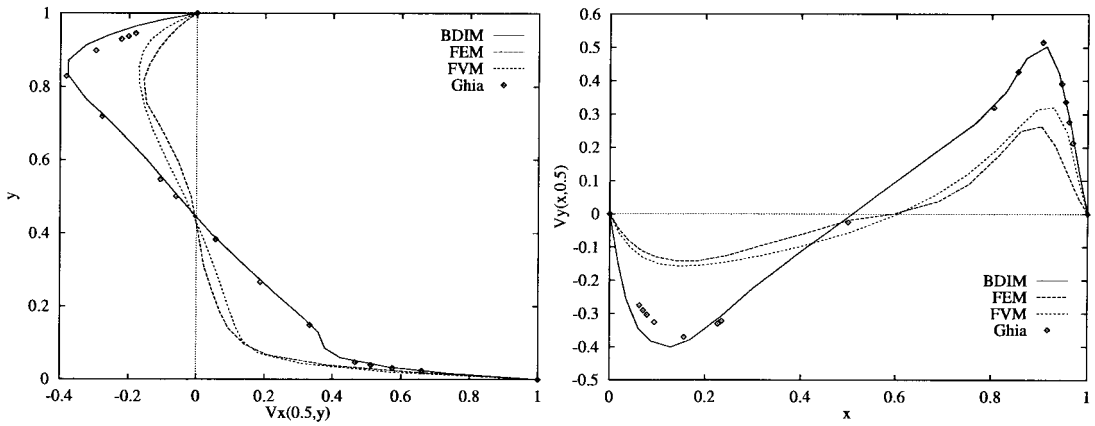

Figure 11. Driven cavity at $Re = 1000$. Comparison of BDIM results with FVM, FEM and benchmark solutions by Ghia, horizontal velocity at $x = 0.5$ (left) and vertical velocity at $y = 0.5$ (right). Grid density 21×21 dof with a ratio longest/shortest = 6.

At $Re = 1000$, Figures 11 and 12, the advantage of the BDIM is most evident. The FEM and FVM results at these grid densities failed to predict flow circumstances. Again, the BDIM profiles agree well with the benchmark solution at both grid densities (compare Figures 11 and 12).

6. LAMINAR MIXED CONVECTION IN A DRIVEN CAVITY

6.1. Problem definition

The basic aim of this problem study is the influence of the buoyancy force on the velocity and temperature distribution in a driven cavity.

Consider a driven cavity flow, with a moving and heating bottom boundary at $y = 0$. The dimensionless temperature $\bar{T} = 1$ is set on this moving boundary and $\bar{T} = 0$ on the rest. At the driven wall, the buoyancy force has the maximum effect and pulls the fluid in the direction of the driving wall movement, so there is a very thin and negligible viscous sublayer. We can treat these phenomena as a Couette flow [18] and set boundary conditions directly at the moving wall (see Figure 13).

The results of different *Gr* numbers are compared with the results obtained by Lee and Chen [13] calculated by the FEM only for a non-equidistant 10×10 grid with a ratio of longest/shortest equal to 10. No nodalization analysis is presented in the original paper by Lee.

6.2. Results

The BDIM nodalization analysis shows a slow convergence of average Nusselt number values at each wall, see Tables IX, X and XI. The BDIM results on different grids differ because of the different lengths of the modelled moving boundary. In vertex points $x = 0$, $y = 0$ and $x = 1$, $y = 0$, the boundary conditions are undefined, either velocity in the x-direction or the temperature is set for a moving wall or a static wall. After a detailed investigation, a static wall with $v_x = 0$ and $T = 0$ are chosen. With this decision made, the actual modelled moving boundary is longer with a higher grid density, and, consequently, there is a higher rate of heat

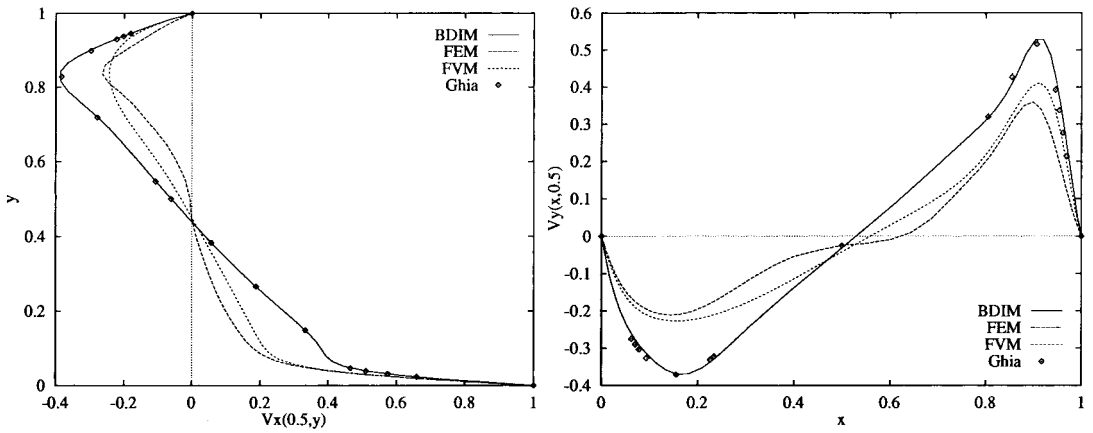

Figure 12. Driven cavity at $Re = 1000$. Comparison of BDIM results with FVM, FEM and benchmark solutions by Ghia, horizontal velocity at $x = 0.5$ (left) and vertical velocity at $y = 0.5$ (right). Grid density 41×41 dof with a ratio longest/shortest = 6.

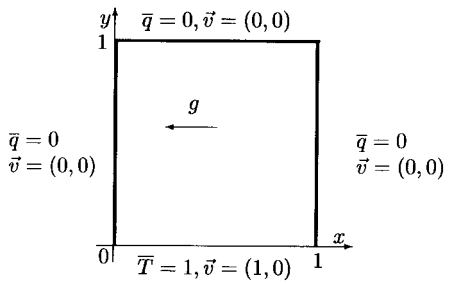

Figure 13. Geometry and boundary conditions for mixed convection in a driven cavity.

Table IX. Mixed convection at $Re = 100$, $Gr/Re^2 = 0.0$

	Lee	BDIM			
$\overline{Nu}$	10×10	6×6	10×10	12×12	20×20
$x = 0$	2.342	2.621	2.666	2.734	3.085
$y = 1$	0.453	0.514	0.562	0.566	0.605
$x = 0$	4.881	4.648	5.498	5.635	5.821
Σ	7.676	7.783	8.726	8.935	9.511
$y = 0$	7.728	7.784	8.726	8.935	9.511

Table X. Mixed convection $Re = 100$, $Gr/Re^2 = 0.1$

	Lee	BDIM			
$\overline{Nu}$	10×10	6×6	10×10	12×12	14×14
$x = 0$	2.328	2.597	2.662	2.730	3.079
$y = 1$	0.504	0.565	0.623	0.626	0.614
$x = 0$	4.980	4.715	5.562	5.702	5.852
Σ	7.812	7.877	8.847	9.058	9.545
$y = 0$	7.868	7.878	8.846	9.059	9.545

Table XI. Mixed convection $Re = 100$, $Gr/Re^2 = 1$

	Lee	BDIM			
$\overline{Nu}$	10×10	6×6	10×10	12×12	20×20
$x = 0$	2.278	2.572	2.588	2.736	3.044
$y = 1$	0.763	0.876	0.966	0.905	0.965
$x = 0$	5.360	5.018	5.967	5.974	6.283
Σ	8.401	8.466	9.521	9.615	10.292
$y = 0$	8.473	8.466	9.520	9.616	10.292

transfer going through it. With the increasing Gr number, the rate of heat transfer is increased slightly.

There is a slight disagreement between the BDIM results and those of Lee. The flux balance error of Lee is approximately 0.5%, while that for the BDIM is less than 0.01%.

7. CONCLUSIONS

A new mixed boundary element approach in BDIM was successfully tested through several test cases. The accuracy of the BDIM results are significantly higher in comparison with the FEM and FVM for the same grid density, but higher CPU consumption is the price that has to be paid. In order to make the BDIM more economical, a different solver for an overdetermined matrix should be developed.

ACKNOWLEDGMENTS

The authors wish to thank the Ministry of Science and Technology of Republic Slovenia for financial support.

REFERENCES

1. J.C. Wu, 'Problem of general viscous flow', in *Developments in BEM*, Vol. 2, Elsevier, London, 1982, Ch. 2.
2. L. Škerget, A. Alujevič, C.A. Brebbia and G. Kuhn, 'Natural and forced convection simulation using the velocity–vorticity approach', in *Topics in Boundary Element Research*, Vol. 5, Springer, Berlin, 1989, Ch. 4, pp. 49–86.
3. G. Guj and F. Stella, 'A vorticity–velocity method for the numerical solution of 3D incompressible flows', *J. Comput. Phys.*, **106**, 286–298 (1993).
4. L. Škerget and Z. Rek, 'Boundary domain integral method for using a velocity–vorticity formulation', *Eng. Anal. Bound. Elem.*, **15**, 359–370 (1995).
5. I. Žagar and L. Škerget, 'The numerical simulation of non-linear separation columns by boundary-domain integral formulation', *Comput. Chem. Eng.*, **19**, 785–790 (1995).
6. Z. Rek and L. Škerget, 'Boundary element method for steady 2D high-Reynolds number flow', *Int. J. Numer. Methods Fluids*, **19**, 343–361 (1994).
7. I. Žagar and L. Škerget, 'The stability investigation of the combined boundary domain integral formulation', *ZAMM*, **73**, 928–931 (1993).
8. M. Hriberšek and L. Škerget, 'Iterative methods in solving Navier–Stokes equations by the boundary element method', *Int. J. Numer. Methods Fluids*, **39**, 115–139 (1996).
9. L. Škerget, 'Mixed convection cavity flows', *BEM-I9*, Rim, 1997, pp. 505–514.
10. P.K. Banerjee and R. Butterfield, *Boundary Element Methods in Engineering Science*, McGraw-Hill, UK, 1981.
11. U. Ghia, K.N. Ghia and C.T. Shin, 'High-*Re* solutions for incompressible flow using the Navier–Stokes equations and a multigrid method', *J. Comput. Phys.*, **48**, 387–411 (1982).
12. G.D.V. Davis, 'Natural convection of air in a square cavity: a bench mark numerical solution', *Int. J. Numer. Methods Fluids*, **3**, 249–264 (1983).
13. S.C. Lee and C.-K. Chen, 'Finite element solutions of laminar and turbulent mixed convection in a driven cavity', *Int. J. Numer. Methods Fluids*, **23**, 47–64 (1996).
14. LAPACK, http://www.netlib.org/lapack/
15. C.C. Paige and M.A. Saunders, 'LSQR: sparse linear equations and least-squares problems', *ACM Trans. Math. Software*, **8**, 195–209 (1982).
16. FIDAP 7.62. Example Manual 7.0, Fluid Dynamics International, April 1993.
17. TASCflow, Version 2.4.1-3, Advanced Scientific Computing Ltd., 1996.
18. V.S. Arpaci and P.S. Larsen, *Convection Heat Transfer*, Prentice-Hall, London, 1984.

